Applied Materials Today 37 (2024) 102144

Contents lists available at ScienceDirect

Applied Materials Today

journal homepage: www.elsevier.com/locate/apmt

Hybrid functional membranes through layer-by-layer assembly of $Ti_3C_2T_x$ MXene and gelatin-stabilized calcium phosphate nanospheres

Gelareh Rezvan [a], Farivash Gholamirad [a], Mary K. Walden [b], Yonghui Wang [c,d], Piao Zhao [c,e], Monirosadat Sadati [a], Tong-Chuan He [c], Nader Taheri-Qazvini [a,b,*]

[a] Department of Chemical Engineering, University of South Carolina, Columbia, SC 29208, United States
[b] Department of Biomedical Engineering, University of South Carolina, Columbia, SC 29208, United States
[c] Molecular Oncology Laboratory, Department of Orthopaedic Surgery and Rehabilitation Medicine, The University of Chicago Medical Center, Chicago, IL 60637, USA
[d] Department of Endocrinology, Shanghai Jiaotong University School of Medicine, Shanghai 200000, China
[e] Department of Orthopaedic Surgery, the First Affiliated Hospital of Chongqing Medical University, Chongqing 400016, China

ARTICLE INFO

Keywords:
MXene
Layer-by-layer assembly
Amorphous calcium phosphate
Hybrid membrane
Good stability

ABSTRACT

MXene-based membranes exhibit promising properties for various applications; however, pure MXene membranes lack sufficient environmental stability and mechanical strength. This work demonstrates that incorporating gelatin-stabilized amorphous calcium phosphate (Gel-ACP) nanospheres into MXene membranes via layer-by-layer assembly significantly enhances flexibility and mechanical strength while retaining electrical conductivity. A pressure-assisted stacking technique was introduced to efficiently fabricate membranes with tunable thickness not achievable through single filtration steps. The Gel-ACP nanospheres, synthesized by co-precipitation of calcium phosphate within gelatin solution, provided a ductile and cytocompatible reinforcement that augmented the properties of the MXene matrix. Direct mixing of the components led to particle aggregation and non-uniform dispersion. In contrast, controlled layer-by-layer nanostructuring maintained membrane conductivity around 10^2 Scm^{-1} while dramatically improving mechanical integrity. The optimized hybrid membranes exhibited specific electromagnetic shielding effectiveness of ~21,000 $dBcm^2g^{-1}$ and withstood over 90 kPa vacuum pressure without rupture, six times higher than pure MXene membranes. Cytocompatibility was confirmed by the proliferation of human mesenchymal stem cells on the membranes. Moreover, the layered membrane exhibited excellent adhesion to bone-mimicking structures, indicating potential utility for bone tissue engineering. Overall, this work provides new design principles for engineering hybrid membranes through controlled multicomponent assembly to overcome intrinsic limitations and impart multifunctionality.

1. Introduction

Two-dimensional (2D) transition metal carbides and nitrides, known as MXenes, have emerged as a promising class of materials for applications ranging from energy storage to water purification [1]. Since the first Ti_3C_2 MXene was synthesized in 2011 [2], extensive research has focused on exploiting the unique properties of MXene nanoflakes, including metallic conductivity, hydrophilicity, and abundant surface terminations [3–6]. Of particular interest is the assembly of MXene nanoflakes into freestanding films or membranes, which enable numerous functional applications that are not feasible with dispersed flakes [7–9].

Vacuum-assisted filtration provides a simple and scalable approach for the fabrication of MXene membranes from a colloidal suspension of delaminated flakes [10]. The resultant membranes exhibit advantageous properties for separation, sensing, electromagnetic shielding, and biomedical applications [11–15]. However, pristine MXene membranes also suffer from drawbacks, including poor stability, low flexibility, and minimal functionality beyond the inherent attributes of MXene [16].

Introducing supplementary nanoscale building blocks has been shown to impart useful functionalities absent from pure MXene membranes, such as enhanced mechanical strength, flexibility, and environmental stability [9,17-20]. For example, a composite membrane combining $Ti_3C_2T_x$ MXene flakes and poly(vinyl alcohol) displayed a

* Corresponding author.
E-mail address: ntaheri@cec.sc.edu (N. Taheri-Qazvini).

https://doi.org/10.1016/j.apmt.2024.102144
Received 1 January 2024; Received in revised form 2 February 2024; Accepted 22 February 2024
Available online 29 February 2024

four-fold tensile strength improvement over pristine MXene [18]. While a diverse array of nanoparticles and polymers have been examined as additives [9,17-25], the opportunity to develop hybrid layered films combining 2D MXene nanosheets with spherical polymer/inorganic hybrid nanoparticles remains relatively underexplored despite prospects for synergy. Tailored hybrid nanoparticles can potentially offer distinct advantages if rationally assembled into nanostructured composites with MXene.

Here, we investigate the integration of gelatin-stabilized amorphous calcium phosphate (Gel-ACP) hybrid nanospheres within $Ti_3C_2T_x$ MXene membranes via layer-by-layer assembly to fabricate layered hybrid films. The functional groups on gelatin molecules enable controlled mineralization of the amorphous and metastable calcium phosphate phase, forming cytocompatible and flexible nanoparticles without triggering hydroxyapatite crystallization [26–28]. This imparts a soft/hard, organic/inorganic hybrid character, contrasting many other nanoparticles in $Ti_3C_2T_x$ MXene-based composite films. As the gelatin gradually degrades under physiological conditions, the slow release of calcium/phosphate ions may enhance osteoconductivity [29,30]. Thus, Gel-ACP nanoparticles hold prospective value for bone regeneration applications. The deformable hybrid nanospheres can also enhance MXene membrane mechanics compared to rigid building blocks. The abundance of surface terminations on MXene available for bridging via nanoscale interactions, e.g., hydrogen bonding and electrostatic, is expected to allow durable interface formation without compromising packing density or flexibility. Moreover, the alternating conductive MXene layers and non-conductive Gel-ACP interlayers generate interfaces that can effectively attenuate electromagnetic radiation via different mechanisms [31]. Finally, the capacity to uniformly distribute Gel-ACP throughout MXene layers via layer-by-layer assembly promises performance exceeding simple blending.

We specifically focus on examining direct material mixing versus designed nanostructuring to highlight how controlled layer-by-layer assembly of MXene with Gel-ACP governs hybrid membrane properties by modulating interfacial interactions. We further demonstrate a pressure-assisted stacking approach to efficiently construct thicker layered membranes without disrupting cohesion. Ultimately, by combining complementary $Ti_3C_2T_x$ MXene 2D nanosheets and spherical Gel-ACP nanoparticles in a layered architecture, the hybrid films display improved mechanical integrity, electrical conductivity, competitive EMI shielding effectiveness, and acquisition of advantageous biophysical attributes. Our results underscore the benefits of controlled nanostructure assembly and open new possibilities for thin films with precisely tailored multifunctionality.

2. Experimental

2.1. Materials

For this study, we utilized Gelatin type B (from bovine skin, 225 bloom), calcium chloride dihydrate ($CaCl_2{\cdot}2H_2O$), potassium phosphate dibasic (K_2HPO_4), hydroxyapatite nano-powder, and sodium hydroxide, all sourced from Sigma-Aldrich. Lithium fluoride (99 % LiF) and hydrochloric acid (HCl) were procured from Millipore Sigma. The MAX phase Ti_3AlC_2 was acquired from Carbon-Ukraine. Mesenchymal Stem Cell Medium and Human bone marrow-derived mesenchymal stem cells (hBMSCs) were obtained from ScienCell Research Laboratories (HMSC-bm; Carlsbad, CA). All chemicals were utilized as received, with no further purification required. All sample preparations and experiments employed milli-Q water (18.2 MΩ·cm, 25 °C).

2.2. Synthesis of Gel-ACP hybrid nanoparticles

The Gel-ACP hybrid nanoparticles were synthesized via controlled precipitation of calcium phosphate in an aqueous medium. The pH of a 0.6 wt% gelatin solution was adjusted to 8 using a 1 M sodium hydroxide solution. The nanoparticles were formed by sequential adding $CaCl_2$ (20 mM) and K_2HPO_4 (10 mM) solutions dropwise (at a rate of 1 $mL.min^{-1}$) to the vigorously stirred gelatin solution. The final dispersion contained $CaCl_2$, K_2HPO_4, and gelatin at concentrations of 10 mM, 5 mM, and 3 $mg.mL^{-1}$, respectively. Sodium hydroxide was added to increase the dispersion pH to 10, preventing nanoparticle precipitation. After synthesis, the nanoparticles were freeze-dried for three days and stored for characterization analysis, while a portion of the dispersion was diluted threefold and used immediately for hybrid membrane preparation.

2.3. Preparation of MXene nanoflakes

The $Ti_3C_2T_X$ MXene flakes were prepared by selectively etching Al atomic layers from the MAX phase, as detailed in previous research [7]. In brief, to achieve minimally invasive layer delamination, the MAX phase was dispersed in 20 ml of etching solution (9 M HCl containing 1.5 g of LiF) and stirred for 28 h at 45 ℃. The delaminated MXene flakes were isolated from the acidic medium and residual MAX phase through repeated centrifugation. The MXene flake dispersion was stored at −70 ℃ in an argon-purged vial for future use.

2.4. Fabrication and characterization of MXene/Gel-ACP hybrid membranes

The freestanding MXene-based membranes were fabricated using vacuum-assisted filtration through a PVDF substrate (pore size of 0.45 μm). The multilayered MXene thin film was formed by filtering an 18 mL dispersion (1 mg/mL). Hybrid membranes were prepared using either a direct mixing (DM) or a layer-by-layer (LBL) approach. For the DM membrane fabrication, equal volumes of MXene and Gel-ACP dispersions (1 $mg.mL^{-1}$) were mixed under vigorous stirring and filtered. In contrast, the LBL hybrid membranes were fabricated via the controlled assembly of MXene and Gel-ACP by adding alternating layers of the dispersions (1 $mg.mL^{-1}$). LBL membranes consisted of 6 layers, each containing 2 mg of MXene or Gel-ACP. As each applied layer lost water under vacuum, the next layer was poured on top of the previous one. To enhance functionality by increasing thickness, three prepared LBL membranes were laminated together by placing the wet surface of the freshly prepared membrane in contact with the dried surface of the previously prepared one and applying controlled pressure to assemble them, forming an integrated thicker membrane. Consequently, each resulting membrane contained 18 mg of MXene plus 18 mg of nanospheres in the case of hybrid membranes. All three membrane groups were air-dried and easily peeled off from the substrate.

2.5. Biocompatibility with human mesenchymal stem cells (MSCs)

Human bone marrow-derived mesenchymal stem cells (hBMSCs) were maintained in the Mesenchymal Stem Cell Medium. Subconfluent hBMSCs were infected with an adenoviral vector expressing GFP, Ad-GFP (Refs PMID: 37397535; PMID: 34522718; PMID: 37443106), for 24 h. Meanwhile, MXene and LBL hybrid membranes (3 × 3 mm) were sterilized, placed in 12-well cell culture plates, and pre-incubated in complete DMEM medium for 2 h. The Ad-GFP infected cells were collected and seeded onto MXene and LBL hybrid membranes at $\sim 10^4$ cells per seeding and maintained with complete DMEM medium in the 37℃ and 5 % CO_2 incubator. The culture medium was changed every two days. GFP fluorescence signal was recorded on days 1, 3, 5, and 7 after seeding. Each scaffold was done in triplicate.

2.6. Characterization methods

Field-emission scanning electron microscopy (FE-SEM, Zeiss Gemini500) and transmission electron microscopy (TEM; Hitachi HT7800) were used to characterize the morphology of Gel-ACP, MXene nanoflakes, and the membranes. Dynamic light scattering (Zetasizer

Nano-ZS, Malvern Instruments) was used to measure the size and zeta potential of the Gel-ACP nanoparticles and MXene nanoflakes. The internal structure of Gel-ACP was examined with small-angle X-ray scattering (SAXS) analysis (Ganesha-SAXSLab). X-ray diffraction (XRD) analysis (Rigaku miniflex, equipped with a copper k-α source with $\lambda =$ 0.154 nm) was used to determine the layered structure of the membranes and the amorphous nature of Gel-ACP. The gelatin and ACP content of Gel-ACP nanoparticles were measured using thermogravimetric analysis (TGA 550, TA Instruments). Membrane properties, including electrical conductivity, electromagnetic interference shielding, and mechanical strength under vacuum pressure, were tested using 4-point probe (Ossila T2001A3) measurements, network vector analyzer (ZVA67, Rohde & Schwarz), and a home-built apparatus, respectively. Further details on experimental methods are provided in the Supplementary Information.

3. Results and discussion

3.1. Characterization

The modified MILD method was employed as a top-down exfoliation route to delaminate single-layer MXene nanoflakes from the Ti_3AlC_2 MAX phase (Fig. 1-a,b). Electron microscopy imaging directly observed the morphology and size distribution of the single-layer MXene nanoflakes, revealing an average lateral size of approximately 1.5 μm (Fig. 1-c). The transparency of nanosheets in TEM images confirmed their ultrathin structure, while the hexagonal symmetry obtained by selected area electron diffraction (SAED) revealed the polycrystalline structure of MXene (Fig. 1-d) [8]. These observations indicate the success of the etching and delamination process. Due to the terminational functional group, the MXene surface in water possesses a permanent negative charge of −45 mV at neutral pH, preventing homo-aggregation and ensuring dispersion stability (Fig. S2, Supplementary Information). The surface chemistry of MXene nanosheets allows interaction with other species, including spherical gelatin nanoparticles.

In nature, hard tissues such as bone and tooth form based on organic-inorganic hybrid materials [32]. Inspired by nature, we fabricated gelatin-calcium phosphate spherical hybrid nanoparticles via controlled precipitation of calcium phosphate in the presence of a gelatin solution. Calcium ions can interact with negatively charged carboxyl and hydroxyl groups of gelatins, causing configurational changes in the chain. The addition of phosphate ions initiates the nucleation of ACP nanoparticles within the gelatin matrix [32,33]. This process forms globular gelatin matrix nanoparticles with an average diameter of 230 nm (PDI < 0.2), stabilizing the ACP (Gel-ACP) (Fig. 1-e; Fig. S3, Supplementary Information).

To define the calcium phosphate polymorphs, X-ray diffraction (XRD) analysis was performed on the dried hybrid nanoparticles (Fig. 1-f). Contrary to the HA, a crystalline reference sample that exhibited Bragg diffraction with a characteristic peak at 32–35°, the XRD pattern of the hybrid nanoparticles showed no distinct peaks except for a characteristic hump at 30°. This confirms the amorphous structure of Gel-ACP [30,34,35], indicating that the gelatin chains successfully prevent the ACP crystallization. Encapsulated in the gelatin matrix, the ACP retains its amorphous structure even for two weeks under ambient conditions (Fig. S4, Note S1, Supplementary Information).

To determine the composition of the Gel-ACP hybrid nanoparticles, thermogravimetric analysis was performed in an air atmosphere. The obtained data for Gel-ACP was compared to gelatin and HA to quantify the weight percentage of the mineral phase in the hybrid nanoparticles

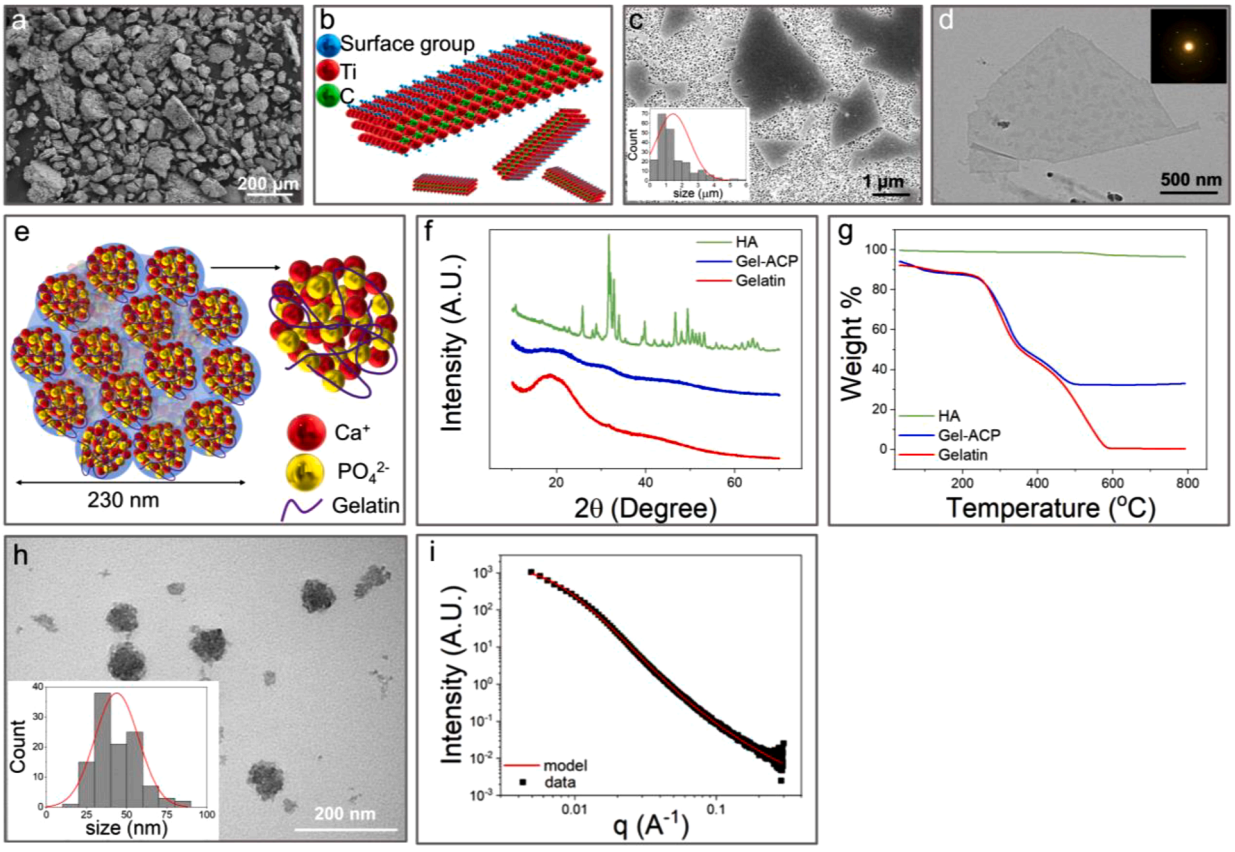

Fig. 1. (a) FESEM image of initial Ti_3AlC_2 MAX particles, (b) Schematic of $Ti_3C_2T_x$ MXene nanoflakes structure; Morphology of individual MXene nanoflakes by using (C) FESEM imaging (inset: MXene lateral size distribution) and (d) TEM imaging (inset: MXene hexagonal symmetry obtained by the SAED), (e) schematic of Gel-ACP hybrid nanoparticles structure, (f) XRD pattern and (g) TGA thermogram of Gel-ACP, gelatin and HA, (h) TEM imaging of Gel-ACP hybrid nanoparticles, and (i) SAXS profile of Gel-ACP nanoparticles. The solid line represents fitting unified model on the experimental data.

(Fig. 1-g). Heating up to 200 °C, both gelatin and Gel-ACP powder showed a weight loss of approximately 10–13 wt%, which can be attributed to the evaporation of the free and bound water. Considering the thermal stability of the HA and ACP phases and assuming that all the gelatin chains would burn out of the system at 600℃, the dried Gel-ACP hybrid particles were found to be composed of 55±11 wt% mineral phase, with the remaining weight attributed to gelatin.

The dried Gel-ACP nanospheres, with an average diameter of 40 nm, were directly observed using transmission electron microscopy (TEM) (Fig. 1-h). The dehydration of the nanoparticles justifies the difference in size measured by DLS and observed through imaging. Furthermore, the small dark objects inside the nanoparticles are the denser ACP nanoclusters encapsulated within the gelatin matrix. This observation is in agreement with the previous observations that confirmed the polymer-stabilized ACP particles are made out of aggregation of smaller nanostructures (Fig. 1-e) [36–38].

To gain a better understanding of the internal structure of these Gel-ACP hybrid nanoparticles, small-angle X-ray scattering analysis was performed on the dried Gel-ACP powder. Fig. 1-i depicts the plot of scattering intensity versus scattering vector, q. To analyze the elemental unit of the structure, the collected scattering intensity should be disintegrated to identify the contribution from each structural element [39]. The unified fit approach proposed by G. Beaucage was used for this purpose (Note S2, Supplementary Information) [40]. The model fitting on SAXS data confirmed the hierarchical structure of Gel-ACP with a sphere-like structure of 52 nm diameter composed of 10 nm oblates structure of ACP encompassed by gelatin chain, which aligns with the imaging observations (Fig. 1-e,h).

The fabrication of a freestanding membrane involves the use of vacuum-assisted filtration, an effective method to deposit individual MXene nanoflakes from a dispersion into a compact and aligned structure (Fig. 2-a). A hybrid MXene-based membrane can also be prepared by filtering a stable, uniformly blended dispersion [41,42]. However, achieving a stable dispersion of multiple nanoparticles is not always straightforward, as interparticle interactions can lead to hetero-aggregation and precipitation [7].

Upon direct mixing of Gel-ACP and MXene, even at low concentrations, hydrogen bonds, and van der Waals forces form large aggregates (Fig. 2-b; Fig. S5, Supplementary Information). This aggregation prevents the fully aligned and densely packed assembly of nanoflakes during the filtration process, resulting in a brittle hybrid membrane that restricts its performance (Fig. 2-c).

On the other hand, depositing sequential layers of components offers an easy and practical approach to forming a multilayer structure. This allows the design of advanced hybrid membranes with specific features by incorporating ultra-thin layers of nanomaterials (Fig. 2-d) [43,4]. In this study, the layer-by-layer deposition of Gel-ACP and MXene provided a freestanding, rollable, foldable, and flexible hybrid membrane (Fig. 2-e,f; Movie S1, Supplementary Information).

While vacuum-assisted filtration is a reasonable and straightforward method for fabricating MXene-based hybrid membranes, it can be time-consuming when creating thick layered membranes with multiple component layers. We have developed a simple yet effective method for fabricating integrated thick membranes by utilizing controlled pressure

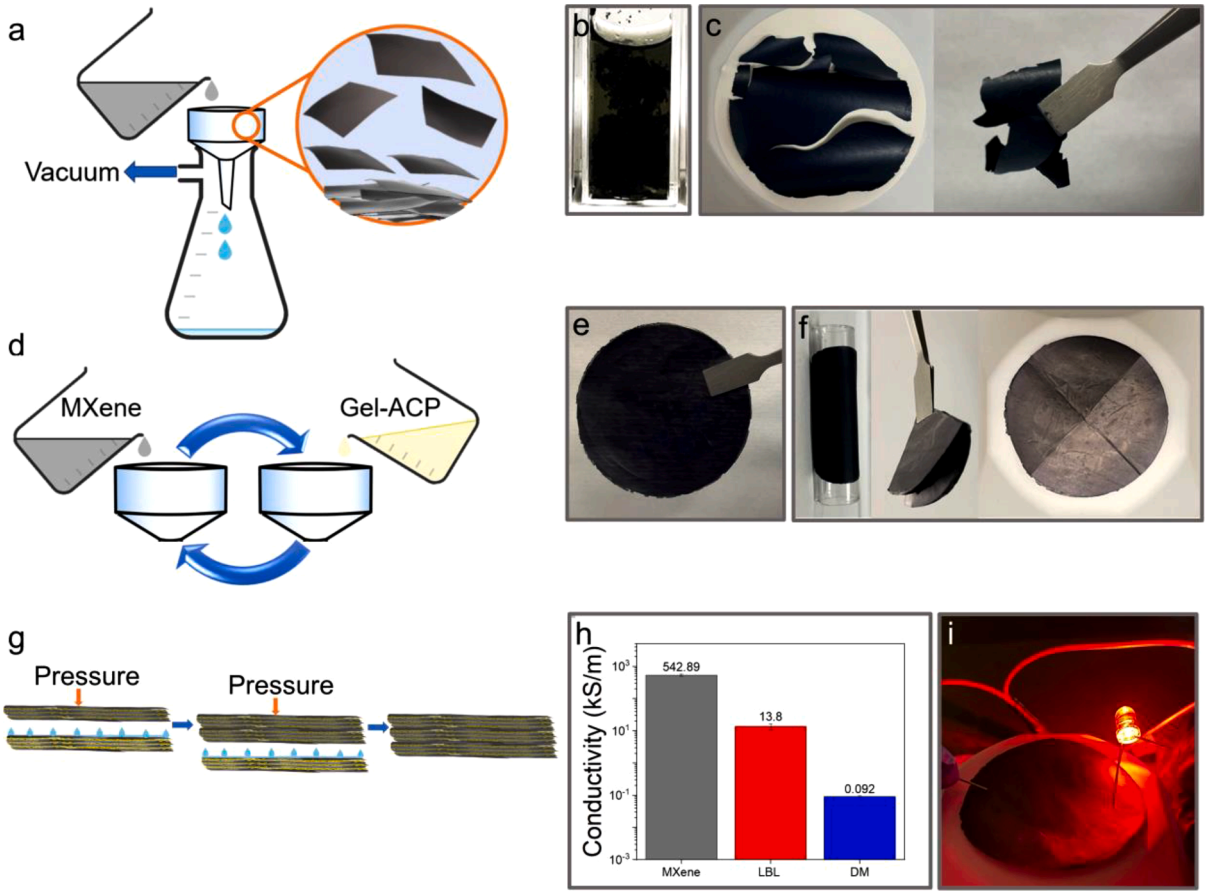

Fig. 2. (a) Schematic of vacuum-assisted filtration setup, (b) photograph of hetero-aggregates of Gel-ACP and MXene upon mixing at concentration of 1 mg.mL^{-1}, (c) Hybrid membrane prepared by direct mixing method, (d) schematic of alternative vacuum-assisted filtration for preparing LBL hybrid membrane, (e) free-standing LBL hybrid membrane, (f) rollability and foldability of LBL hybrid membrane, (g) schematic of the method used to attach freshly prepared LBL membrane to the dried surface of the previously prepared one to increase the thickness, (h) electrical conductivity of MXene-based membranes, and (i) LBL hybrid membrane in an electrical circuit lighten up a light bulb.

to attach prepared thin membranes to each other. In this approach, the air-dried surface of a previously prepared membrane is carefully placed on the wet surface of a freshly prepared membrane. A pressure of 1.5 kPa is then applied to facilitate the assembly of the membranes, which are left to dry afterward. This technique exploits the remaining water molecules on the membrane surface to enable the diffusion of MXene nanoflakes and the formation of a uniform layer at the membranes' interface. The method allows the attachment of an unlimited number of thin membranes, enabling precise control over the desired membrane thickness. Here, we applied this technique to attach three LBL-prepared membranes, each containing 6 mg of MXene, to fabricate a hybrid membrane with the same 18 mg MXene content as the pristine MXene and DM membranes (Fig. 2-g). This pressure-assisted assembly approach aligns with the water-assisted welding concept recently introduced by Wang et al. [10], where water droplets act as local melting-like points to weld MXene membranes.

As anticipated, the pristine MXene membrane displayed substantial electrical conductivity around 5000 S/cm. Yet, the hybrid DM membrane's conductivity was markedly decreased by a factor of 5000 due to interparticle interactions disrupting the MXene network. In contrast, The LBL hybrid membrane, combining Gel-ACP and MXene while exhibiting reduced conductivity relative to pristine MXene (Fig. 2-h,i), nonetheless surpasses the DM membrane's conductivity considerably. Its conductivity remains high enough for practical use in a variety of applications, such as electromagnetic interference (EMI) shielding and electrically stimulated cellular growth [45].

Our EMI shielding measurements revealed promising performance for the LBL MXene/Gel-ACP membrane, with an average shielding effectiveness of 37.6 dB in the X-band frequency range (8–12 GHz) (Fig. S6). To further evaluate the competitiveness of our nanoengineered membrane, we surveyed prior reports focused explicitly on layer-by-layer assembled and vacuum-filtered MXene composite films [21-25, 46-68]. This enabled direct comparison to highly relevant layered architectures fabricated by analogous methods. The LBL MXene/Gel-ACP membrane achieves an EMI shielding effectiveness normalized by thickness and density (SSE/t) of 20,964 $dBcm^2g^{-1}$ (Fig. 3), among the highest performing values reported for MXene-based layered structures. In another comparison, this SSE/t greatly exceeds recently published MXene/polyacrylic acid/amorphous calcium carbonate hydrogel composites, which share resemblances in composition [69].

We attribute the excellent EMI attenuation to multiple factors stemming from the membrane nanoarchitecture. The interfaces between MXene and Gel-ACP layers create an impedance mismatch, serving as interaction sites to promote the dissipation of electromagnetic waves via multiple internal reflections [15,70]. The LBL assembly method enhances this effect over direct material mixing. Additionally, the moderate electrical conductivity enables sufficient conductive loss while avoiding excessive reflection. The durable layered arrangement combines the advantages of MXene flakes and gelatin-stabilized amorphous calcium phosphate nanospheres, yielding excellent structural stability for reliable attenuation. Consequently, considering the concurrent improvements in critical properties, these complementary 2D MXene nanosheets and polymer-based hybrid spherical nanoparticles can be effectively exploited for multifunctional hybrid membrane fabrication.

Microstructural analysis: Cross-sectional observation of the MXene and LBL hybrid membranes, utilizing electron microscopy imaging, highlighted the architectural differences. The MXene membrane demonstrated a well-aligned stacking of nanoflakes, forming a structure of approximately 6.5 μm in thickness (Fig. 4-a). Contrastingly, the LBL hybrid membrane showcased alternating layers of MXene and Gel-ACP with a slightly higher total thickness of about 8.5 μm. The chemical element mapping of Ti, Ca, and P corroborated the presence of these distinct layers (Fig. 4-b).

X-ray diffraction (XRD) analysis further validated these structural characteristics. MXene membranes exhibited (001) peaks suggestive of a preferred stacking orientation of the nanoflakes perpendicular to the membrane surface (Fig. 4-c). Analyzing the highest intensity (002) peak location yielded an interlayer distance of approximately 2.8 Å, a value consistent with previously reported ranges [71,72]. Notably, the (002) peak position remained unchanged for the LBL hybrid membrane, indicating that the introduction of Gel-ACP layers did not interfere with the intrinsic structure of the MXene layers.

However, a sharp decrease in the (002) peak intensity for the LBL hybrid membrane suggests a reduction in the population of fully aligned MXene flakes. This reduction could stem from interparticle interactions at the layer interfaces. Remarkably, the DM hybrid membrane showed no detectable (002) peak. Instead, a shift towards lower angles was observed, denoting an increased interlayer distance. This phenomenon verifies that hetero-aggregation of Gel-ACP and MXene hinders the full alignment of MXene nanoflakes during the vacuum-assisted filtration process, leading to a less compact packing.

Mechanical Strength Assessment: The mechanical robustness of thin

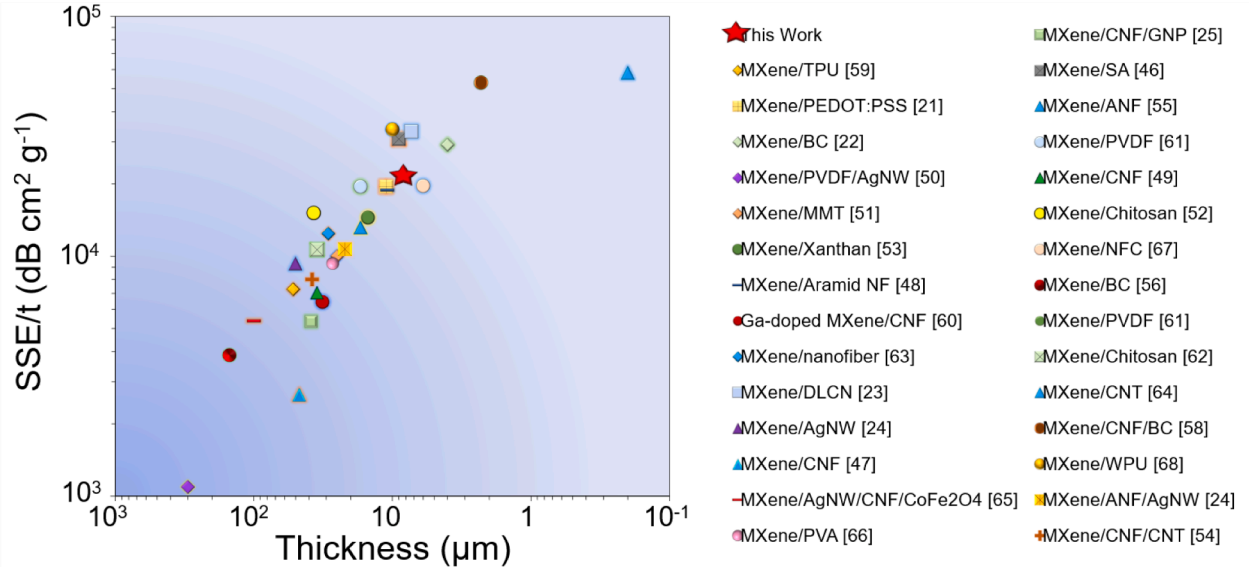

Fig. 3. Comparison of specific EMI shielding effectiveness of MXene/Gel-ACP layer-by-layer membranes with other layer-by-layer assembled and vacuum-filtered $Ti_3C_2T_x$ MXene-based composite films.

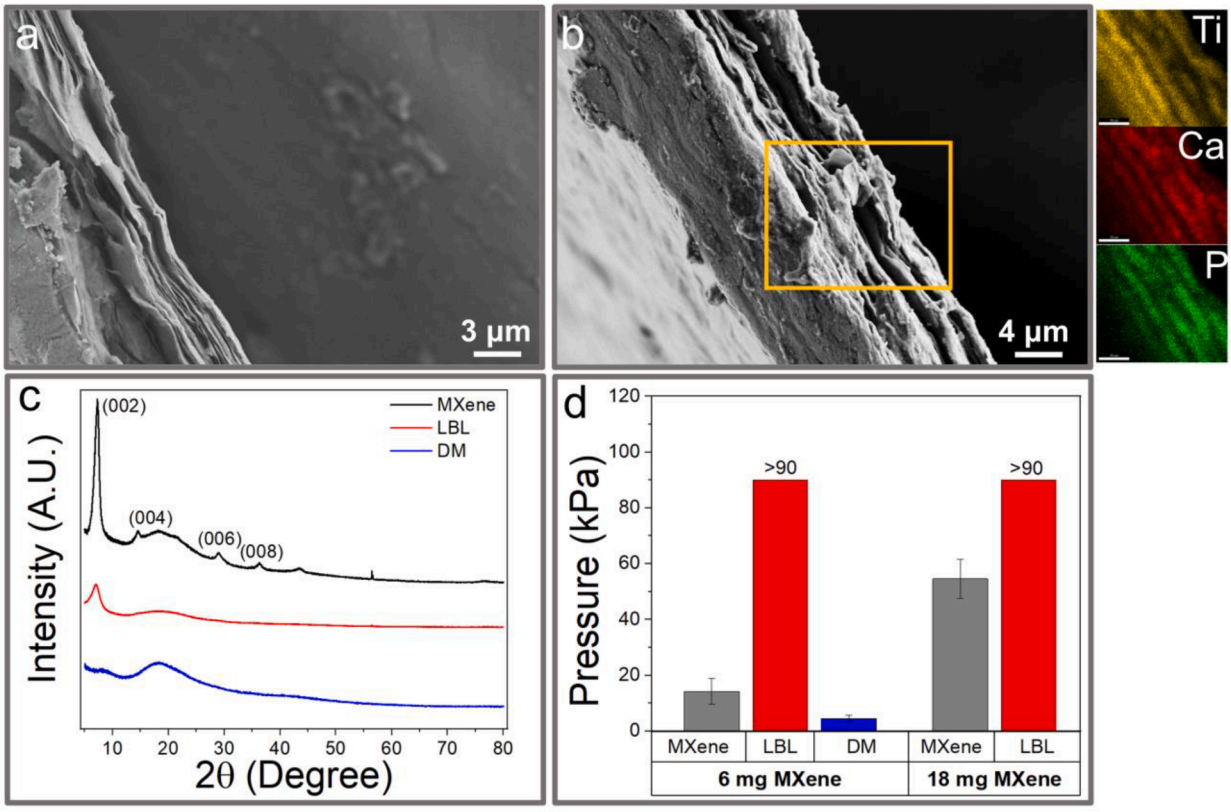

Fig. 4. Cross sectional FESEM images of (a) MXene membrane and (b) LBL hybrid membrane and the corresponding chemical element distribution obtained by EDS (scale bar = 10 μm), (c) XRD pattern and (d) negative burst pressure of MXene-based membranes.

membranes significantly influences their applicability across diverse fields. Previous research has successfully enhanced the tensile strength of MXene membranes through the incorporation of supplementary materials such as graphene oxide [41]. For instance, S. Wan et al. [17] reported a nine-fold boost in tensile strength and a twofold increase in elongation for a hybrid membrane comprising MXene, sodium alginate, and calcium ions compared to a pristine MXene membrane.

In this study, our aim was to examine the mechanical strength across the thickness of the designed membranes, particularly the influence of the integrated Gel-ACP layers. For this purpose, a homemade setup was employed to subject the membranes to vacuum or negative pressure. The maximum applied negative pressure before the membrane burst or tore was recorded as the membrane's strength along its thickness (Fig. S1, Video S2–3, Supplementary Information).

To investigate the effect of thickness on membrane structure, two distinct membrane thicknesses were prepared: one containing 6 mg of MXene and the other containing 18 mg of MXene. The pristine MXene membrane made up of 6 mg of nanoflakes, demonstrated resilience to a negative pressure of 14.3 ± 4.7 kPa (Fig. 4-d). The tolerance to negative pressure markedly increased to 54.6 ± 7.0 kPa with a threefold increment in membrane thickness.

The DM hybrid membrane, while brittle, exhibited significantly weaker mechanical properties under vacuum conditions. On the contrary, the LBL hybrid membrane, containing either 6 mg or 18 mg of MXene nanosheets, showed exceptional resilience, remaining intact even at a negative pressure of 90 kPa, the upper limit of our experimental setup.

These findings highlight the critical role of both membrane thickness and the molecular interactions within the membrane in determining its mechanical strength. The synergy between MXene nanoflakes and Gel-ACP nanospheres at the membrane interfaces significantly enhances durability by creating strong, robust layers. The enhancement in the membrane's strength could potentially be attributed to the gelatin's flexibility, which might facilitate the even distribution of stress across the MXene layers through shear lag effects [73]. Additionally, this flexibility allows the gelatin to absorb significant deformations during crack growth, potentially dissipating energy through the breaking of sacrificial bonds, which could contribute to improved resistance to fractures in the membrane. Also, MXene nanoflakes bridging by the free calcium ions might play a role in the enhanced mechanical properties that necessitates further detailed investigation. In addition to molecular-scale interactions, the method we used to increase the thickness of the LBL membrane effectively maintains the structural integrity without creating weak points at the attachment sites.

3.2. *Membrane biocompatibility and potential for bone tissue engineering applications*

The MXene/Gel-ACP hybrid membranes exhibit several promising characteristics that indicate potential utility for bone tissue engineering applications such as guided bone regeneration (GBR). MXene itself possesses inherent biocompatibility due to its component elements of Ti, C, O, and other elements commonly present in the human body [74]. Additionally, MXene nanosheets have demonstrated broad-spectrum antibacterial effects against both Gram-positive and Gram-negative bacteria [75]. This could aid bone regeneration applications by preventing infection and biofilm formation. MXene nanoflakes have also exhibited bioactivity related to their strong calcium ion affinity, which may provide nucleation sites to promote bone cell mineralization [76, 77]. Overall, the nanocomposite integrates the advantageous properties of MXene and Gel-ACP to yield a cytocompatible, mechanically robust, and bioactive membrane architecture.

Cytocompatibility with human mesenchymal stem cells (hMSCs) was demonstrated by robust cell adhesion, spreading, and proliferation on

the membrane surface over 7 days of culture (Fig. 5). The cells displayed numerous filopodial extensions indicative of healthy morphology and cytoskeletal organization. Viability and growth were maintained on both pure MXene and the hybrid membranes, indicating the incorporation of Gel-ACP did not impede the inherent cell compatibility of MXene.

The durable layered nanostructure could potentially prevent premature collapse of the membrane prior to tissue ingrowth, which is a risk for highly porous scaffolds [78,79]. The aligned MXene sheets provide mechanical strength, while the gelatin component adds ductility. This robustness could enable the maintenance of an open geometry favorable for cell and tissue infiltration.

Furthermore, gelatin is expected to dissolve in a controlled manner under physiological conditions, gradually releasing bioactive calcium and phosphate ions from the amorphous calcium phosphate nanoparticles [28,80]. This controlled solubilization of key osteogenic components may stimulate endogenous bone growth. Degradation and bioactive ion release properties could be tuned based on the gelatin concentration and chemical crosslinking.

Notably, the MXene/Gel-ACP hybrid membrane demonstrated strong adhesion to the surface of an artificial bone substrate, even supporting more than 20 times its weight without detachment (Fig. 6a). Scanning electron microscopy revealed that the nanorough morphology and topological features of the membrane surface enable mechanical interlocking with the simulated bone material (Fig. 6b). This implies sufficient initial adhesive strength to remain fixed over bone defects, which is an essential requirement for the GBR applications. GBR involves using a barrier membrane to facilitate the restoration of bone in damaged areas resulting from trauma, disease, or surgical resections [40]. For clinical success, the GBR membrane must remain securely in place, separating the bone defect from surrounding soft tissues for the duration of bone regeneration. If the membrane detaches or collapses into the defect space, non-osseous cell types can infiltrate the area, compromising bone formation [43,81]. The measured adhesion strength of the hybrid membrane suggests the feasibility of maintaining stable placement over bone defects. Additionally, incubation in phosphate-buffered saline at 37 °C for 3 weeks, used to mimic physiological conditions, did not alter the integrity or properties of the membrane (Fig. 6c). This implies satisfactory in vitro stability and bioresistance for the timescales involved in bone healing and regeneration processes.

The MXene/Gel-ACP hybrid membranes exhibit morphological features and properties promising for GBR applications. The nanoscale surface roughness of MXene enables tight early bone fixation, while the ductile gelatin-ACP layers provide mechanical durability, flexibility, and possible osteogenic bioactivity through controlled calcium and phosphate ion release upon gelatin degradation. These combinations make the nanostructured hybrid membranes attractive candidates for GBR compared to existing products and membranes composed of only synthetic polymers. Further in vivo testing will be necessary to fully evaluate the performance of GBR, including assessments of biodegradation, bone regeneration capacity, host response, and benchmarking against commercially available GBR membranes. Overall, this work establishes a promising new nanocomposite material system and membrane fabrication approach for bone engineering.

4. Conclusion

MXene-based membranes have garnered great interest across diverse applications, including electromagnetic interference shielding, energy

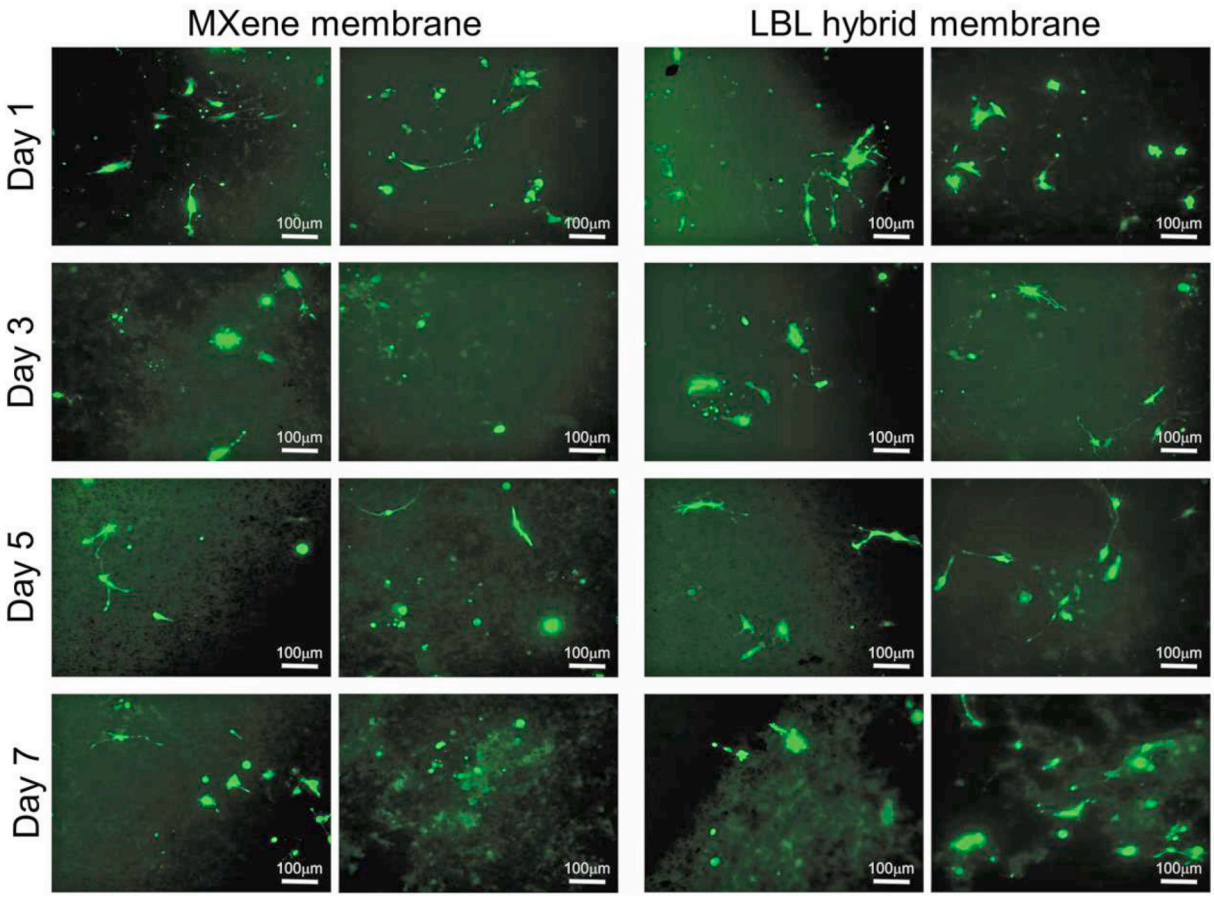

Fig. 5. Documented GFP signal at different time intervals after seeding Human MSCs, infected with Ad-GFP, on MXene and LBL hybrid membrane.

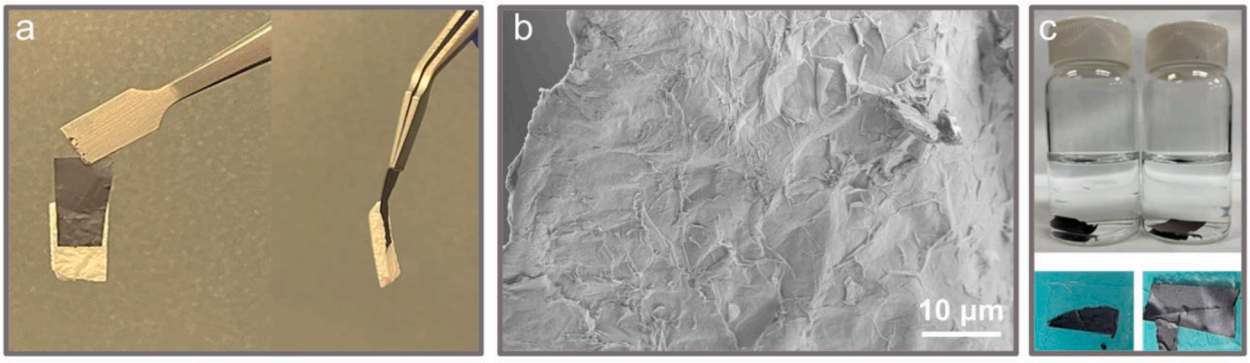

Fig. 6. (a) adhesiveness of LBL hybrid membrane to the wet surface of artificial bone (composed of gelatin chains and HA nanoparticles), (b) FESEM image of LBL hybrid membrane's surface, (c) stability of MXene (left) and LBL hybrid membranes (right) in the BS solution at 37℃ after three weeks.

storage, water treatment, and biomedicine. This work demonstrates that the incorporation of gelatin-stabilized amorphous calcium phosphate nanospheres in MXene membranes via a layer-by-layer assembly technique significantly enhances mechanical integrity and durability while retaining useful electrical conductivity. The Gel-ACP nanospheres provided a ductile, tissue-compatible component that augmented the properties of the MXene nanoflake matrix.

Direct mixing of the two nanoparticulate components resulted in particle aggregation and a disordered membrane microstructure. In contrast, the controlled layer-by-layer deposition maintained aligned MXene stacking while integrating reinforcing Gel-ACP layers, synergistically enhancing membrane robustness. The optimized hybrid membranes exhibited remarkable mechanical resilience, withstanding vacuum pressures up to 90 kPa without rupture. This represents a six-fold and ten-fold increase compared to pure MXene membranes and direct mixed membranes, respectively.

Furthermore, a pressure-assisted stacking technique was introduced to efficiently produce thick layered membranes without compromising nanostructure or properties. This membrane bonding approach addresses a key limitation in the fabrication of MXene-based with thicknesses exceeding what is achievable through a single filtration cycle.

In addition to mechanical reinforcement, the nanostructured hybrid membranes demonstrated emergent functionality. The combination of MXene and Gel-ACP layers exhibited an excellent specific electromagnetic shielding effectiveness (SSE/t) of 20,964 $dBcm^2g^{-1}$ across X-band frequencies. Furthermore, the cytocompatibility was retained, supporting the proliferation of human mesenchymal stem cells.

This work elucidates design guidelines and criteria for engineering multifunctional hybrid membranes through the rational selection and assembly of complementary nanoscale building blocks. The layer-by-layer fabrication approach established here provides a versatile platform for incorporating new functionalities into MXene membranes while overcoming intrinsic limitations.

However, while our study provides a thorough characterization of hybrid MXene-based membranes, it is important to recognize that there are limitations in fully substantiating their potential applications. This work offers an initial yet promising foundation for more in-depth investigations into practical uses. For example, the robust and flexible nature of these hybrid membranes, along with their demonstrated capacity for stem cell attachment and proliferation, suggests potential utility in bone regeneration. Specifically, the favorable initial adhesion strengths to bone-mimicking scaffolds underscore prospects within guided bone regeneration applications. Nevertheless, to conclusively validate these applications, further studies, particularly in vivo evaluations in animal models, are essential. Also, flexible films with simultaneously high mechanical integrity, electrical conductivity, and cytocompatibility could find potential roles as stimulate-responsive elements aiding regeneration in neuronal and cardiac tissue engineering setups. Additionally, the excellent electromagnetic interference attenuation may warrant trials replacing metallic signal-blocking components in appliances where maintaining nontoxicity, low weight, and nonflammability is paramount, such as medical devices. These future investigations will be critical in determining the full scope and effectiveness of these membranes in real-world applications.

Additional experimental details are provided, including the zeta potential measurements of MXene nanoflakes and the size distribution analysis of Gel-ACP nanoparticles. The design and setup of the burst pressure measurement system are shown. XRD and SAXS data are presented for Gel-ACP nanoparticles, along with details on the unified fitting approach used to characterize the nanostructure of Gel-ACP. Phase behavior of the MXene/Gel-ACP system and EMI shielding performance data for the layer-by-layer MXene/Gel-ACP hybrid membrane are also included.

CRediT authorship contribution statement

Gelareh Rezvan: Writing – original draft, Visualization, Investigation, Data curation. **Farivash Gholamirad:** Writing – original draft, Investigation. **Mary K. Walden:** Investigation. **Yonghui Wang:** Investigation. **Piao Zhao:** Investigation. **Monirosadat Sadati:** Resources, Writing – review & editing. **Tong-Chuan He:** Writing – review & editing, Supervision, Resources. **Nader Taheri-Qazvini:** Writing – review & editing, Supervision, Resources, Funding acquisition, Conceptualization.

Declaration of competing interest

The authors declare that they have no known competing financial interests or personal relationships that could have appeared to influence the work reported in this paper.

Data availability

The datasets generated and analyzed during the current study are available from the corresponding author on reasonable request.

Acknowledgments

This research was supported by funding from the National Science Foundation, USA (award # 2238908). We appreciate Prof. G. Wang from the Electrical Engineering Department at the University of South Carolina for providing access to the vector network analyzer.

Supplementary materials

Supplementary material associated with this article can be found, in the online version, at doi:10.1016/j.apmt.2024.102144.

References

[1] B. Anasori, Y. Gogotsi, MXenes: trends, growth, and future directions, Graph. 2D Mater. 7 (3–4) (2022) 75–79.
[2] G. Shan, Z. Ding, Y. Gogotsi, Two-dimensional MXenes and their applications, Front. Phys. 18 (1) (2023) 1–5.
[3] C. Qiao, H. Wu, X. Xu, Z. Guan, W. Ou-Yang, Electrical conductivity enhancement and electronic applications of 2D Ti3C2Tx MXene materials, Adv. Mater. Interfaces 8 (24) (2021) 1–19.
[4] Y. Feng, H. Liu, W. Zhu, L. Guan, X. Yang, A.V. Zvyagin, Y. Zhao, C. Shen, B. Yang, Q. Lin, Muscle-inspired MXene conductive hydrogels with anisotropy and low-temperature tolerance for wearable flexible sensors and arrays, Adv. Funct. Mater. 31 (46) (2021).
[5] H. Huang, R. Jiang, Y. Feng, H. Ouyang, N. Zhou, X. Zhang, Y. Wei, Recent development and prospects of surface modification and biomedical applications of MXenes, Nanoscale 12 (3) (2020) 1325–1338.
[6] M. Naguib, V.N. Mochalin, M.W. Barsoum, Y. Gogotsi, 25th anniversary article: MXenes: a new family of two-dimensional materials, Adv. Mater. 26 (7) (2014) 982.
[7] F. Gholamirad, N. Taheri-Qazvini, Three-dimensional porous Ti3C2Tx MXene-based hybrids formed by charge-driven assembly, Chem. Mater. 33 (24) (2021) 9560–9570.
[8] X. Zhao, X.J. Zha, L.S. Tang, J.H. Pu, K. Ke, R.Y. Bao, Z.y. Liu, M.B. Yang, W. Yang, Self-assembled core-shell polydopamine@MXene with synergistic solar absorption capability for highly efficient solar-to-vapor generation, Nano Res. 13 (1) (2020) 255–264.
[9] Y. Fu, J. Zhang, H. Lin, A. Mo, 2D titanium carbide(MXene) nanosheets and 1D hydroxyapatite nanowires into free standing nanocomposite membrane: in vitro and in vivo evaluations for bone regeneration, Mater. Sci. Eng. C 118 (December 2019) (2021) 111367.
[10] J. Wang, Y. Liu, Y. Yang, J. Wang, H. Kang, H. Yang, D. Zhang, Z. Cheng, Z. Xie, H. Tan, Z. Fan, A weldable MXene film assisted by water, Matter 5 (3) (2022) 1042–1055.
[11] Small Science 2021 - Huang - MXene-Based Membranes for Separation Applications.pdf.
[12] R. Thankappan, K.G. Vasanthakumari, U.M. Uzma Sulthana, MXene-coated flexible PVDF membrane as wearable strain sensor, J. Mater. Sci. 33 (32) (2022) 24542–24549.
[13] B. Lu, Z. Zhu, B. Ma, W. Wang, R. Zhu, J. Zhang, 2D MXene nanomaterials for versatile biomedical applications: current trends and future prospects, Small 17 (46) (2021) 1–38.
[14] K. Khorsand Kazemi, S. Hu, O. Niksan, K.K. Adhikari, N.R. Tanguy, S. Li, M. Arjmand, M.H. Zarifi, Low-profile planar antenna sensor based on Ti3C2Tx MXene membrane for VOC and humidity monitoring, Adv. Mater. Interfaces 9 (13) (2022) 1–11.
[15] B. Zhou, Z. Zhang, Y. Li, G. Han, Y. Feng, B. Wang, D. Zhang, J. Ma, C. Liu, Flexible, robust, and multifunctional electromagnetic interference shielding film with alternating cellulose nanofiber and MXene layers, ACS. Appl. Mater. Interfaces 12 (4) (2020) 4895–4905.
[16] MXenes: From Discovery to Applications of Two-Dimensional Metal Carbides and Nitrides, CRC Press, 2023.
[17] S. Wan, X. Li, Y. Wang, Y. Chen, X. Xie, R. Yang, A.P. Tomsia, L. Jiang, Q. Cheng, Strong sequentially bridged MXene sheets, Proc. Natl. Acad. Sci. 117 (44) (2020) 27154–27161.
[18] Z. Ling, C.E. Ren, M.Q. Zhao, J. Yang, J.M. Giammarco, J. Qiu, M.W. Barsoum, Y. Gogotsi, Flexible and conductive MXene films and nanocomposites with high capacitance, Proc. Natl. Acad. Sci. U.S.A. 111 (47) (2014) 16676–16681.
[19] J. Lu, L. Cheng, C. Liao, P. Jia, L. Song, B. Wang, Y. Hu, Ultrathin and mechanically robust mussel byssus-inspired MXene@Aramid nanofibers materials with superior endurance in harsh environments for tunable EMI shielding performance, Adv. Mater. Interfaces 9 (5) (2022) 2101359.
[20] C. Wang, R. Cheng, P.X. Hou, Y. Ma, A. Majeed, X. Wang, C. Liu, MXene-carbon nanotube hybrid membrane for robust recovery of Au from trace-level solution, ACS. Appl. Mater. Interfaces 12 (38) (2020) 43032–43041.
[21] R. Liu, M. Miao, Y. Li, J. Zhang, S. Cao, X. Feng, Ultrathin biomimetic polymeric Ti3C2Tx MXene composite films for electromagnetic interference shielding, ACS Appl. Mater. Interfaces 10 (51) (2018) 44787–44795.
[22] Y. Wan, P. Xiong, J. Liu, F. Feng, X. Xun, F.M. Gama, Q. Zhang, F. Yao, Z. Yang, H. Luo, Ultrathin, strong, and highly flexible Ti3C2Tx MXene/bacterial cellulose composite films for high-performance electromagnetic interference shielding, ACS Nano 15 (5) (2021) 8439–8449.
[23] B. Li, S. Luo, S. Anwer, V. Chan, K. Liao, Heterogeneous films assembled from Ti3C2Tx MXene and porous double-layered carbon nanosheets for high-performance electromagnetic interference shielding, Appl. Surf. Sci. 599 (2022) 153944.
[24] Z. Ma, S. Kang, J. Ma, L. Shao, Y. Zhang, C. Liu, A. Wei, X. Xiang, L. Wei, J. Gu, Ultraflexible and mechanically strong double-layered aramid nanofiber–Ti3C2Tx mxene/silver nanowire nanocomposite papers for high-performance electromagnetic interference shielding, ACS Nano 14 (7) (2020) 8368–8382.
[25] Q. Chu, H. Lin, M. Ma, S. Chen, Y. Shi, H. He, X. Wang, Cellulose nanofiber/graphene nanoplatelet/MXene nanocomposites for enhanced electromagnetic shielding and high in-plane thermal conductivity, ACS Appl. Nano Mater. 5 (5) (2022) 7217–7227.
[26] J. Zhao, Y. Liu, W.B. Sun, H. Zhang, Amorphous calcium phosphate and its application in dentistry, Chem. Cent. J. 5 (1) (2011) 1–7.
[27] A. Lotsari, A.K. Rajasekharan, M. Halvarsson, M. Andersson, Transformation of amorphous calcium phosphate to bone-like apatite, Nat. Commun. 9 (1) (2018).
[28] V.M. Wu, V. Uskoković, Is there a relationship between solubility and resorbability of different calcium phosphate phases in vitro? Biochim. Biophys. Acta 1860 (10) (2016) 2157–2168.
[29] Y. Feng, D. Wu, J. Knaus, S. Keßler, B. Ni, Z. Chen, J. Avaro, R. Xiong, H. Cölfen, Z. Wang, A bioinspired gelatin–amorphous calcium phosphate coating on titanium implant for bone regeneration, Adv. Healthc. Mater. (2023) 2203411.
[30] C. Zhao, N.T. Qazvini, M. Sadati, Z. Zeng, S. Huang, A.L. De La Lastra, L. Zhang, Y. Feng, W. Liu, B. Huang, B. Zhang, Z. Dai, Y. Shen, X. Wang, W. Luo, B. Liu, Y. Lei, Z. Ye, L. Zhao, D. Cao, L. Yang, X. Chen, A. Athiviraham, M.J. Lee, J. M. Wolf, R.R. Reid, M. Tirrell, W. Huang, J.J. De Pablo, T.C. He, A pH-triggered, self-assembled, and bioprintable hybrid hydrogel scaffold for mesenchymal stem cell based bone tissue engineering, ACS Appl. Mater. Interfaces 11 (9) (2019) 8749–8762.
[31] Y. Liu, Y. Wang, N. Wu, M. Han, W. Liu, J. Liu, Z. Zeng, Diverse structural design strategies of mxene-based macrostructure for high-performance electromagnetic interference shielding, Nanomicro Lett. 15 (1) (2023) 240.
[32] S. Sun, L.B. Mao, Z. Lei, S.H. Yu, H. Cölfen, Hydrogels from amorphous calcium carbonate and polyacrylic acid: bio-inspired materials for “mineral plastics”, Angew. Chem. Int. Ed. 55 (39) (2016) 11765–11769.
[33] A. Bhattacharyya, G. Janarthanan, T. Kim, S. Taheri, J. Shin, J. Kim, H.C. Bae, H. S. Han, I. Noh, Modulation of bioactive calcium phosphate micro/nanoparticle size and shape during in situ synthesis of photo-crosslinkable gelatin methacryloyl based nanocomposite hydrogels for 3D bioprinting and tissue engineering, Biomater. Res. 26 (1) (2022) 1–17.
[34] X. Niu, Z. Liu, F. Tian, S. Chen, L. Lei, T. Jiang, Q. Feng, Y. Fan, Sustained delivery of calcium and orthophosphate ions from amorphous calcium phosphate and poly (L-lactic acid)-based electrospinning nanofibrous scaffold, Sci. Rep. 7 (1) (2017) 45655.
[35] R.A. Ramli, R. Adnan, M.A. Bakar, S.a.M. Masudi, Synthesis and characterisation of pure nanoporous hydroxyapatite, J. Phys. Sci. 22 (1) (2011) 20–37.
[36] X. Zhang, Y. Li, X. Sun, A. Kishen, X. Deng, X. Yang, H. Wang, C. Cong, Y. Wang, M. Wu, Biomimetic remineralization of demineralized enamel with nano-complexes of phosphorylated chitosan and amorphous calcium phosphate, J. Mater. Sci. 25 (12) (2014) 2619–2628.
[37] Z. Chen, S. Cao, H. Wang, Y. Li, A. Kishen, X. Deng, X. Yang, Y. Wang, C. Cong, H. Wang, X. Zhang, Biomimetic remineralization of demineralized dentine using scaffold of CMC/ACP nanocomplexes in an in vitro tooth model of deep caries, PLoS ONE 10 (1) (2015) 1–19.
[38] M. Lin, H. Liu, J. Deng, R. An, M. Shen, Y. Li, X. Zhang, Carboxymethyl chitosan as a polyampholyte mediating intrafibrillar mineralization of collagen via collagen/ACP self-assembly, J. Mater. Sci. Technol. 35 (9) (2019) 1894–1905.
[39] T. Koga, T. Hashimoto, M. Takenaka, K. Aizawa, N. Amino, M. Nakamura, D. Yamaguchi, S. Koizumi, New insight into hierarchical structures of carbon black dispersed in polymer matrices: a combined small-angle scattering study, Macromolecules 41 (2) (2008) 453–464.
[40] G. Beaucage, Approximations leading to a unified exponential/power-law approach to small-angle scattering, J. Appl. Crystallogr. 28 (6) (1995) 717–728.
[41] F. Wang, Z. Wang, S. Wang, X. Meng, Y. Jin, N. Yang, J. Sunarso, S. Liu, Mechanically intensified and stabilized MXene membranes via the combination of graphene oxide for highly efficient osmotic power production, J. Memb. Sci. 647 (2022).
[42] Y. Yang, Y. Han, J. Zhao, W. Que, 2D/1D MXene/MWCNT hybrid membrane-based evaporator for solar desalination, Materials 15 (3) (2022) 1–7.
[43] K.R. Zhang, H.L. Gao, X.F. Pan, P. Zhou, X. Xing, R. Xu, Z. Pan, S. Wang, Y. Zhu, B. Hu, D. Zou, S.H. Yu, Multifunctional bilayer nanocomposite guided bone regeneration Membrane, Matter 1 (3) (2019) 770–781.
[44] Y. Wang, T.T. Li, B.C. Shiu, X. Zhang, H.K. Peng, C.W. Lou, J.H. Lin, MXene-decorated nanofiber film based on layer-by-layer assembly strategy for high-performance electromagnetic interference shielding, Appl. Surf. Sci. 574 (October 2021) (2022) 151552.
[45] F. Gholamirad, J. Ge, M. Sadati, G. Wang, N. Taheri-Qazvini, Tuning the self-assembled morphology of Ti(3)C(2)T(x) MXene-based hybrids for high-performance electromagnetic interference shielding, ACS. Appl. Mater. Interfaces 14 (43) (2022) 49158–49170.
[46] F. Shahzad, M. Alhabeb, C.B. Hatter, B. Anasori, S. Man Hong, C.M. Koo, Y. Gogotsi, Electromagnetic interference shielding with 2D transition metal carbides (MXenes), Science 353 (6304) (2016) 1137–1140.
[47] B. Zhou, Z. Zhang, Y. Li, G. Han, Y. Feng, B. Wang, D. Zhang, J. Ma, C. Liu, Flexible, robust, and multifunctional electromagnetic interference shielding film with alternating cellulose nanofiber and MXene layers, ACS. Appl. Mater. Interfaces 12 (4) (2020) 4895–4905.
[48] F. Xie, F. Jia, L. Zhuo, Z. Lu, L. Si, J. Huang, M. Zhang, Q. Ma, Ultrathin MXene/aramid nanofiber composite paper with excellent mechanical properties for efficient electromagnetic interference shielding, Nanoscale 11 (48) (2019) 23382–23391.
[49] W.-T. Cao, F.-F. Chen, Y.-J. Zhu, Y.-G. Zhang, Y.-Y. Jiang, M.-G. Ma, F. Chen, Binary strengthening and toughening of MXene/cellulose nanofiber composite

paper with nacre-inspired structure and superior electromagnetic interference shielding properties, ACS Nano 12 (5) (2018) 4583–4593.
[50] H. Cheng, Y. Pan, Q. Chen, R. Che, G. Zheng, C. Liu, C. Shen, X. Liu, Ultrathin flexible poly (vinylidene fluoride)/MXene/silver nanowire film with outstanding specific EMI shielding and high heat dissipation, Adv. Compos. Hybrid. Mater. 4 (2021) 505–513.
[51] L. Li, Y. Cao, X. Liu, J. Wang, Y. Yang, W. Wang, Multifunctional MXene-based fireproof electromagnetic shielding films with exceptional anisotropic heat dissipation capability and joule heating performance, ACS. Appl. Mater. Interfaces. 12 (24) (2020) 27350–27360.
[52] F. Liu, Y. Li, S. Hao, Y. Cheng, Y. Zhan, C. Zhang, Y. Meng, Q. Xie, H. Xia, Well-aligned MXene/chitosan films with humidity response for high-performance electromagnetic interference shielding, Carbohydr. Polym. 243 (2020) 116467.
[53] Y. Sun, R. Ding, S.Y. Hong, J. Lee, Y.-K. Seo, J.-D. Nam, J. Suhr, MXene-xanthan nanocomposite films with layered microstructure for electromagnetic interference shielding and Joule heating, Chem. Eng. J. 410 (2021) 128348.
[54] W. Cao, C. Ma, S. Tan, M. Ma, P. Wan, F. Chen, Ultrathin and flexible CNTs/MXene/cellulose nanofibrils composite paper for electromagnetic interference shielding, Nanomicro Lett. 11 (2019) 1–17.
[55] C. Liu, Y. Ma, Y. Xie, J. Zou, H. Wu, S. Peng, W. Qian, D. He, X. Zhang, B.-W. Li, Enhanced electromagnetic shielding and thermal management properties in MXene/aramid nanofiber films fabricated by intermittent filtration, ACS. Appl. Mater. Interfaces 15 (3) (2023) 4516–4526.
[56] H. Liu, Z. Cui, L. Luo, Q. Liao, R. Xiong, C. Xu, C. Wen, B. Sa, Facile fabrication of flexible and ultrathin self-assembled Ti3C2Tx/bacterial cellulose composite films with multifunctional electromagnetic shielding and photothermal conversion performances, Chem. Eng. J. 454 (2023) 140288.
[57] Y. Fu, J. Zhang, H. Lin, A. Mo, 2D titanium carbide (MXene) nanosheets and 1D hydroxyapatite nanowires into free standing nanocomposite membrane: in vitro and in vivo evaluations for bone regeneration, Mater. Sci. Eng. C 118 (2021) 111367.
[58] Z. Zhou, Q. Song, B. Huang, S. Feng, C. Lu, Facile fabrication of densely packed Ti3C2 MXene/nanocellulose composite films for enhancing electromagnetic interference shielding and electro-/photothermal performance, ACS. Nano 15 (7) (2021) 12405–12417.
[59] Q. Gao, Y. Pan, G. Zheng, C. Liu, C. Shen, X. Liu, Flexible multilayered MXene/thermoplastic polyurethane films with excellent electromagnetic interference shielding, thermal conductivity, and management performances, Adv. Compos. Hybrid. Mater. 4 (2021) 274–285.
[60] Y. He, J. Yang, W. Chen, W. Chen, L. Zhao, W. Qi, Gallium-doped MXene/cellulose nanofiber composite membranes with electro/photo thermal conversion property for high performance electromagnetic interference shielding, Chem. Eng. J. 464 (2023) 142565.
[61] Y. Li, B. Zhou, Y. Shen, C. He, B. Wang, C. Liu, Y. Feng, C. Shen, Scalable manufacturing of flexible, durable Ti3C2Tx MXene/Polyvinylidene fluoride film for multifunctional electromagnetic interference shielding and electro/photo-thermal conversion applications, Composites Part B 217 (2021) 108902.
[62] Z. Tan, H. Zhao, F. Sun, L. Ran, L. Yi, L. Zhao, J. Wu, Fabrication of Chitosan/MXene multilayered film based on layer-by-layer assembly: toward enhanced electromagnetic interference shielding and thermal management capacity, Composites Part A 155 (2022) 106809.
[63] Y. Wang, T.-T. Li, B.-C. Shiu, X. Zhang, H.-K. Peng, C.-W. Lou, J.-H. Lin, MXene-decorated nanofiber film based on layer-by-layer assembly strategy for high-performance electromagnetic interference shielding, Appl. Surf. Sci. 574 (2022) 151552.
[64] G.M. Weng, J. Li, M. Alhabeb, C. Karpovich, H. Wang, J. Lipton, K. Maleski, J. Kong, E. Shaulsky, M. Elimelech, Layer-by-layer assembly of cross-functional semi-transparent MXene-carbon nanotubes composite films for next-generation electromagnetic interference shielding, Adv. Funct. Mater. 28 (44) (2018) 1803360.
[65] Z. Guo, P. Ren, F. Yang, T. Wu, L. Zhang, Z. Chen, F. Ren, Robust multifunctional composite films with alternating multilayered architecture for highly efficient electromagnetic interference shielding, Joule heating and infrared stealth, Composites Part B (2023) 110863.
[66] X. Jin, J. Wang, L. Dai, X. Liu, L. Li, Y. Yang, Y. Cao, W. Wang, H. Wu, S. Guo, Flame-retardant poly (vinyl alcohol)/MXene multilayered films with outstanding electromagnetic interference shielding and thermal conductive performances, Chem. Eng. J. 380 (2020) 122475.
[67] X. Xu, S. Wu, J. Cui, L. Yang, D. Liu, Y. Zhang, X. Chen, K. Wu, D. Sun, Insights into the microstructures and reinforcement mechanism of nano-fibrillated cellulose/MXene based electromagnetic interference shielding film, Cellulose 28 (2021) 3311–3325.
[68] Z. Liu, W. Wang, J. Tan, J. Liu, M. Zhu, B. Zhu, Q. Zhang, Bioinspired ultra-thin polyurethane/MXene nacre-like nanocomposite films with synergistic mechanical properties for electromagnetic interference shielding, J. Mater. Chem. C 8 (21) (2020) 7170–7180.
[69] Y. Zhu, J. Liu, T. Guo, J.J. Wang, X. Tang, V. Nicolosi, Multifunctional Ti3C2T x MXene composite hydrogels with strain sensitivity toward absorption-dominated electromagnetic-interference shielding, ACS. Nano 15 (1) (2021) 1465–1474.
[70] F. Jia, J. Dong, X. Dai, Y. Liu, H. Wang, Z. Lu, Robust, flexible, and stable CuNWs/MXene/ANFs hybrid film constructed by structural assemble strategy for efficient EMI shielding, Chem. Eng. J. 452 (September 2022) (2023) 139395.
[71] M. Yi, M. Wang, Y. Wang, Y. Wang, J. Chang, A.K. Kheirabad, H. He, J. Yuan, M. Zhang, Poly (ionic liquid)-armored MXene membrane: interlayer engineering for facilitated water transport, Angew. Chem. 134 (27) (2022) e202202515.
[72] G. Liu, Y. Guo, B. Meng, Z. Wang, G. Liu, W. Jin, Two-dimensional MXene hollow fiber membrane for divalent ions exclusion from water, Chin. J. Chem. Eng. 41 (2022) 260–266.
[73] D.G. Papageorgiou, I.A. Kinloch, R.J. Young, Mechanical properties of graphene and graphene-based nanocomposites, Prog. Mater. Sci. 90 (2017) 75–127.
[74] H. Huang, C. Dong, W. Feng, Y. Wang, B. Huang, Y. Chen, Biomedical engineering of two-dimensional MXenes, Adv. Drug Deliv. Rev. 184 (2022) 114178.
[75] K. Rasool, M. Helal, A. Ali, C.E. Ren, Y. Gogotsi, K.A. Mahmoud, Antibacterial Activity of Ti(3)C(2)Tx MXene, ACS. Nano 10 (3) (2016) 3674–3684.
[76] J. Zhang, Y. Fu, A. Mo, Multilayered titanium carbide MXene film for guided bone regeneration, Int. J. Nanomed. 14 (2019) 10091–10103.
[77] K. Chen, N. Qiu, Q. Deng, M.H. Kang, H. Yang, J.U. Baek, Y.H. Koh, S. Du, Q. Huang, H.E. Kim, Cytocompatibility of Ti(3)AlC(2), Ti(3)SiC(2), and Ti(2)AlN: in vitro tests and first-principles calculations, ACS. Biomater. Sci. Eng. 3 (10) (2017) 2293–2301.
[78] J.E. Barralet, L.L. Wallace, A.J. Strain, Tissue engineering of human biliary epithelial cells on polyglycolic acid/polycaprolactone scaffolds maintains long-term phenotypic stability, Tissue Eng. 9 (5) (2003) 1037–1045.
[79] S. Wu, X. Liu, K.W.K. Yeung, C. Liu, X. Yang, Biomimetic porous scaffolds for bone tissue engineering, Mater. Sci. Eng. R 80 (2014) 1–36.
[80] Q. Xing, K. Yates, C. Vogt, Z. Qian, M.C. Frost, F. Zhao, Increasing mechanical strength of gelatin hydrogels by divalent metal ion removal, Sci. Rep. 4 (2014) 1–10.
[81] M. Retzepi, N. Donos, Guided Bone Regeneration: biological principle and therapeutic applications, Clin. Oral Implants Res. 21 (6) (2010) 567–576.